City Research Online

City St George's, University of London

Citation: Strotos, G., Malgarinos, I., Nikolopoulos, N. & Gavaises, M. (2016). Predicting droplet deformation and breakup for moderate Weber numbers. International Journal of Multiphase Flow, 85, pp. 96-109. doi: 10.1016/j.ijmultiphaseflow.2016.06.001

This is the accepted version of the paper.

This version of the publication may differ from the final published version. To cite this item please consult the publisher's version.

Permanent repository link: https://openaccess.city.ac.uk/id/eprint/15680/

Link to published version: https://doi.org/10.1016/j.ijmultiphaseflow.2016.06.001

Copyright and Reuse: Copyright and Moral Rights remain with the author(s) and/or copyright holders. Copies of full items can be used for personal research or study, educational, or not-for-profit purposes without prior permission or charge, unless otherwise indicated, provided that the authors, title and full bibliographic details are credited, a hyperlink and/or URL is given for the original metadata page and the content is not changed in any way. For full details of reuse please refer to City Research Online policy.

City Research Online: http://openaccess.city.ac.uk/ publications@citystgeorges.ac.uk

Predicting droplet deformation and breakup for moderate Weber numbers

George Strotos[1,a,*], Ilias Malgarinos[1,b], Nikos Nikolopoulos[1,c], ManolisGavaises[1,d]

[1]School of Engineering and Mathematical Sciences, City University London, Northampton Square, EC1V 0HB, London, UK

[a] George.Strotos.1@city.ac.uk

[b] Ilias.Malgarinos.1@city.ac.uk

[c] Nikolaos.Nikolopoulos.1@city.ac.uk

[d] M.Gavaises@city.ac.uk

[*]Corresponding author

Abstract

The present work examines numerically the deformation and breakup of free falling droplets subjected to a continuous cross flow. The model is based on the solution of the Navier-Stokes equations coupled with the Volume of Fluid (VOF) methodology utilized for tracking the droplet-air interface; an adaptive local grid refinement is implemented in order to decrease the required computational cost. Neglecting initially the effect of the vertical droplet motion, a 2D axisymmetric approximation is adopted to shed light on influential numerical parameters. Following that, 3D simulations are

performed which include inertial, surface and gravitational forces. The model performance is assessed by comparing the results against published experimental data for the bag breakup and the sheet thinning breakup regimes. Furthermore, a parametric study reveals the model capabilities for a wider range of Weber numbers. It is proved that the model is capable of capturing qualitatively the breakup process, while the numerical parameters that best predict the experimental data are identified.

Keywords: droplet breakup, VOF, adaptive grid refinement

1 Introduction

The droplet motion, deformation and breakup are interesting phenomena observed in a wide variety of engineering applications including (but not limited) liquid sprays injected in combustion engines. Such phenomena have attracted the interest of scientists while several textbooks and review articles have addressed the relevant processes (see selectively (Clift et al., 1978; Faeth et al., 1995; Gelfand, 1996; Guildenbecher et al., 2009; Michaelides, 2006; Pilch and Erdman, 1987; Theofanous, 2011) among others)

The aerodynamic droplet breakup is induced as a result of an initial droplet-gas relative velocity $U_{rel,0}$, and can be macroscopically characterized with the aid of well-known non-dimensional numbers, namely the Weber number (We), the Reynolds number (Re), the Ohnesorge number (Oh) and the density ratio (ε) (Guildenbecher et al., 2009).These are defined as:

$$We = \frac{\rho_g U_{rel,0}^2 D_0}{\sigma} \quad Re = \frac{\rho_g U_{rel,0} D_0}{\mu_g} \quad Oh = \frac{\mu_l}{\sqrt{\rho_l \sigma D_0}} \quad \varepsilon = \frac{\rho_l}{\rho_g} \tag{1}$$

The viscosity ratio $N = \mu_l/\mu_g$ is also another influential parameter (which, however, can be derived from the above dimensionless numbers), while the Mach number can be important under certain flow conditions, which are not of interest to the present study. For low *Oh* numbers (*Oh*<0.1), the droplet breakup is mainly controlled by the *We* number. Increase of the *We* number results in different regimes namely the vibrational breakup, the bag breakup, the multimode breakup, the sheet stripping (or sheet thinning) and the catastrophic breakup (Guildenbecher et al., 2009). Besides these well-defined breakup modes, the multimode breakup can be divided into intermediate breakup modes such as the bag-stamen (or bag-jet or bag/plume), the dual-bag and the plume/shear (or plume/sheet-thinning) breakup (Guildenbecher et al., 2009). For the non-dimensionalisation of time, the shear breakup timescale $\tau_{sh} = D_0\sqrt{\varepsilon}/U_{rel,0}$ proposed by (Nicholls and Ranger, 1969) is widely used.

Several experimental studies have investigated the droplet breakup. Focusing on the aerodynamic breakup, the shock tube technique and the continuous air jet flow technique have been widely used. The shock tube technique provides a spatially uniform gas velocity by suddenly releasing pressurized gas inside a tube; the droplet deforms due to the flow field following the shock wave. This technique was used in (Hsiang and Faeth, 1992, 1993, 1995), (Chou et al., 1997), (Chou and Faeth, 1998), (Dai and Faeth, 2001) among others. The continuous air jet flow technique examines the breakup of droplets exposed to the influence of an air jet flowing from a nozzle; care is usually taken in order to minimize the boundary layer of the free jet and obtain

a more uniform gas velocity; see selectively (Krzeczkowski, 1980), (Liu and Reitz, 1997), (Lee and Reitz, 2000),(Cao et al., 2007),(Opfer et al., 2012; Opfer et al., 2014), (Flock et al., 2012), (Zhao et al., 2010; Zhao et al., 2013), (Guildenbecher and Sojka, 2011), (Jain et al., 2015) among others. Details for these techniques can be found in (Guildenbecher et al., 2009) among others. These techniques are usually applied to millimeter size droplets under atmospheric conditions; as a result, high liquid/gas density ratios are examined.

Krzeczkowski (Krzeczkowski, 1980) used a continuous air jet to study the breakup of various liquids for *We* numbers in the range 13.5-163 and *Oh*<3 and he was one of the first who represented the breakup regimes in the *Oh*-*We* diagram. He focused on the kinematics of droplet breakup and to the breakup duration and concluded that the viscosity ratio plays a minor role. In a later series of studies, (Hsiang and Faeth, 1992, 1993, 1995) used the shock tube experimental technique to study the droplet breakup at atmospheric conditions. They examined droplets of various liquids covering a wide range of *We*, *Oh* and *Re* numbers (*We*=0.5-600, *Oh*<560, *Re*>300). Their results were also combined with the results of previous works to finally derive the various outcomes as a function of the aforementioned parameters. Drop deformation and breakup regimes were presented in *Oh*-*We* map and represent one of the most detailed graphical representations. Later, the same group published a series of papers examining the temporal properties of secondary breakup in specific breakup regimes (Chou and Faeth, 1998; Chou et al., 1997; Dai and Faeth, 2001). Among them, in (Dai and Faeth, 2001) the intermediate breakup regimes were investigated and they identified the bag/plume breakup for 15<*We*<40 and the plume/shear breakup for 40<*We*<80. The first one is quite similar to the bag-stamen breakup, while the second

represents a transition between the bag/plume and the sheet-thinning breakup in which no bag is formed. (Cao et al., 2007) identified a new breakup mode appearing only in continuous air flow experiments. They called it "dual-bag" and it is observed between the bag/plume and the plume/shear breakup for $28<We<41$. The droplet initially breaks up from its periphery and the remaining core droplet deforms into a bag which breaks up again. (Lee and Reitz, 2000; Liu and Reitz, 1997) studied experimentally the breakup of small diesel droplets (D=69-198μm) at atmospheric temperature and pressures up to 9.2atm, achieving density ratios between 80 and 700; nevertheless this had a small impact on breakup. They had a great contribution in understanding the physical mechanism leading to the shear breakup, by comparing cases with identical *We* numbers and *Re* numbers differing by a factor of almost 3. They concluded that the shear breakup is not ought to shear stresses believed so far, but rather to aerodynamic forces bending the flattened drop's edge and creating a sheet. Thus they proposed the sheet-thinning mechanism verified also by numerical studies mentioned latter in this section (Han and Tryggvason, 2001; Khosla and Smith, 2006; Wadhwa et al., 2007). Recently, (Opfer et al., 2012; Opfer et al., 2014) studied experimentally and theoretically the bag breakup of droplets under a continuous air jet flow. They found a similarity between bag breakup, drop-wall impact and binary droplet collision. (Flock et al., 2012) studied experimentally the droplet breakup in the bag and sheet thinning breakup modes using shadowgraphy to record the instantaneous droplet shape, trajectory and mean velocity, while PIV was used to quantify the gas flow motion around the droplet. They concluded that the structure of the gas-phase wake may not significantly affect the transition between liquid-phase breakup morphologies. The investigations of (Zhao et al., 2010)

performed almost at the same time as the aforementioned ones, examined experimentally and theoretically the bag, bag-stamen and dual-bag breakup regimes. They found that the transition between different bag-type regimes depends on the ratio of maximum cross stream drop diameter to the Rayleigh-Taylor (RT) instability wavelength. Later (Zhao et al., 2013) focused on bag-stamen breakup and found that the stamen can be considered as the wave crest of the RT instability, while the growth of stamen was found to have two stages: an initial exponential growth followed by a spike growth. They also measured the size distribution of the fragment droplets, which have been found to follow the log-normal or gamma distribution functions.

The aforementioned experimental studies provide information regarding the critical *We* numbers leading to different breakup regimes, the duration of the phenomenon and the time that the breakup initiates, the droplet drag coefficient and the size distribution of the droplets after the breakup. It is apparent, however, that there is scattering of the results which is probably ought to the experimental techniques used and the experimental uncertainties. This is more evident for the *We* number ranges corresponding to different breakup modes, which is shown in Fig.1 for low *Oh* numbers below 0.1. In Fig.1a, the basic breakup regimes are shown in which the bag-stamen, dual bag and plume/shear breakup regimes have been merged into an "intermediate" breakup regime; the ranges corresponding to vibrational breakup and the catastrophic breakup are not presented and the maximum *We* number shown is limited to 120. On the top of this figure, the sources used are grouped into review studies, shock tube (S.T.) and continuous air jet flow (C.A.J.) experiments. In Fig.1b, the breakup modes observed in the "intermediate" breakup mode are in detail presented, i.e. the bag-stamen, the dual bag and the plume/shear regimes; for the work

of (Jain et al., 2015) the bag-stamen mode includes also the bag/plume mode which are very similar (Cao et al., 2007). It is clear from Fig.1a that for a given *We* number, one has to consider also other parameters and cannot be certain for the breakup outcome. The scattering of the critical *We* number was also reported in the review study of (Guildenbecher et al., 2009) as also in the works of (Jalaal and Mehravaran, 2012) and (Kékesi et al., 2014). It has also to be noted that the data shown in Fig.1 were collected from studies aiming to define the boundaries between different breakup modes and do not include studies with a different orientation. Considering also these studies creates even more confusion, since the work of (Lee and Reitz, 2000; Liu and Reitz, 1997) identified bag breakup for high *We* numbers equal to 56 and 72 and (Flock et al., 2012) identified sheet thinning breakup at a low *We* number equal to 32.

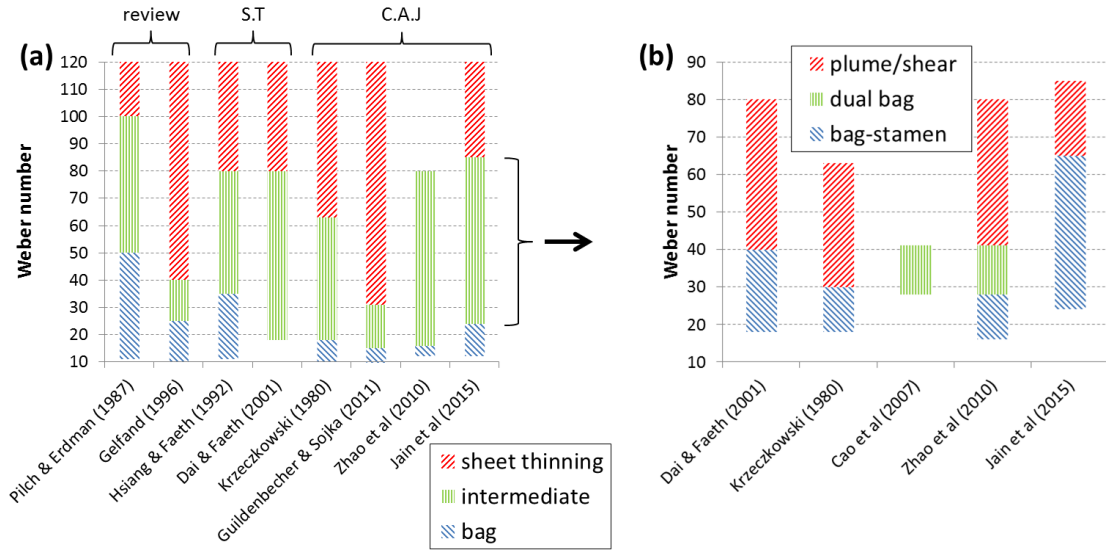

Fig.1: (a) *We* numbers ranges corresponding to the basic breakup regimes (*Oh*<0.1). The breakup modes between the bag breakup and the sheet thinning breakup have been merged into the "intermediate" breakup. In (b) the breakup modes observed into the "intermediate" breakup mode are shown. The data presented in (a) have been

grouped into review studies, shock tube (S.T.) and continuous air jet (C.A.J.) experiments.

Turning now to computational and theoretical studies, a large number of works have been performed, shedding light into the relevant flow processes taking place during droplet breakup; here focus is given on the works referring to the breakup induced by an initial droplet-gas velocity and not the breakup of free falling droplets. (Han and Tryggvason, 2001) studied the breakup of impulsively accelerated droplets by using a front tracking scheme in 2D axisymmetric coordinates. They assumed Diesel engines conditions for low density ratios and examined various combinations of *We* and *Re* numbers. They found that the critical *We* number separating different breakup modes decreases with increasing *Re* number. (Aalburg, 2002) used a 2D axisymmetric Level Set method to study the deformation of droplets for a wide range of *We* and *Oh* numbers at small density ratios and *Re* numbers corresponding to steady-state laminar flow conditions. It was proved that a density ratio above 32 does not affect the droplet deformation and suggested a new regime map by using the coordinates $We^{1/2}/Oh$ – $1/Oh$ as being quite robust with the different breakup boundaries to remain almost constant for $Oh>>1$. (Khosla and Smith, 2006) performed simulations with the VOF methodology in 2D axisymmetric and 3D computational domain. After validating their model qualitatively against experimental data, they concluded that droplet breakup in air crossflow is ought to surface waves instead of the boundary layer stripping mechanism. (Quan and Schmidt, 2006) used a moving mesh interface tracking scheme with mesh adaption techniques to simulate impulsively accelerated droplets. They found that the total drag coefficients are larger than typical steady-state drag coefficients of solid spheres at the same *Re* numbers which is explained by the

large recirculation region behind the deformed droplet. Later (Quan, 2009) used the same model to examine the interaction between two impulsively accelerated droplets as a function of the distance between them. (Wadhwa et al., 2007) studied numerically the transient deformation and drag of decelerating droplets in axisymmetric flows for constant *Re* number. They found that the droplet deformation and the total drag increase with increasing *We* number and decreasing *Oh* number. (Xiao, 2012; Xiao et al., 2012) used a 3D-CLSVOF-LES model to study the primary breakup of liquid jets. To validate their model they examined the secondary droplet breakup in the bag and the sheet-thinning breakup regime (at non-turbulent conditions) showing a good qualitative agreement against experimental photos. (Khare and Yang, 2013) examined the drag coefficients of deforming and fragmenting droplets by using a 3D VOF-DNS methodology with adaptive mesh for a broad range of *We* and *Re* numbers corresponding to bag, multimode and shear breakup conditions. The drag coefficient exhibits a transient behavior, since it initially increases due to droplet deformation and then decreases at the initiation of breakup, while the time-averaged drag coefficient decreases with increasing *We* number. (Jalaal and Mehravaran, 2014) studied numerically and analytically the transient growth of droplet instabilities at conditions corresponding to shear breakup. They employed the VOF methodology in 2D and 3D cases; their model was able to capture the different modes of instabilities occurring during droplet breakup. Besides the Kelvin-Helmholtz instability, the 3D simulations have revealed the presence of one more type of instability, i.e the transverse azimuthal modulation or the Rayleigh-Taylor instability. (Kékesi et al., 2014) used a 3D VOF methodology to study the droplet deformation for low *We* numbers below 12 and the droplet breakup for *We*=20. For the breakup case they examined the effect of density

ratio ($20<\varepsilon<80$), viscosity ratio (0.5-50) and the effect of *Re* number ($20<Re<200$). For the *We*=20 case, depending on the combination of the aforementioned parameters they identified the bag breakup, the shear breakup (despite the low *We* number) and 5 intermediate modes appearing for first time in literature. They proposed a new breakup map in the $Re - N/\sqrt{\varepsilon}$ plane and concluded that any breakup regime can be observed in the proposed map, irrespective of the *We* number, which however contradicts previous experimental and numerical findings. (Jain et al., 2015) studied experimentally and numerically with a 3D VOF methodology the breakup of small water droplets (D=230μm) for *We* numbers in the range 20-120 capturing a wide range of breakup modes. They observed an interesting transition regime between bag and shear breakup for *We* =80 and a different drop size distribution after the breakup for low and high *We* cases; this is probably the most detailed study reported so far. Recently, (Yang et al., 2016) used a variant of the CLSVOF methodology to study the effect of density ratio (ε=10-60) on the droplet breakup for a high We number of 225. They have shown that breakup is affected by the density ratio beyond the ε=32 suggested by (Aalburg, 2002) mainly by altering the topology of the gas phase recirculation, while the effect of density ratio is not monotonic.

A common feature of the most of the aforementioned studies is that the CFD models used were mainly validated qualitatively against experimental observations for the droplet shape at various breakup regimes. They usually examine low density ratios in order to achieve smaller breakup timescale τ_{br}; otherwise a longer physical time has to be simulated as also an even more finer mesh would be required (Jalaal and Mehravaran, 2014). Among them, the 3D VOF simulations obtained with the Gerris code (Jain et al., 2015; Jalaal and Mehravaran, 2014; Khare and Yang, 2013) and the

work of (Yang et al., 2016) with the OpenFoam code are the most impressive. The grid used is dense in the order of 100-200 cells per radius (cpR); thus the underlying physics behind droplet breakup could be revealed. On the other hand, the physical parameters selected (e.g the density and viscosity ratio) do not allow for direct comparison with experimental results and thus they were qualitatively validated; the work of (Jain et al., 2015) is an exception since their model was successfully validated against their own experimental results.

The present work examines numerically the breakup process of droplets at moderate *We* numbers (*We*=13 and 32) subjected to a steady-state cross flow and compares the model results against the detailed experimental measurements of (Flock et al., 2012) for the droplet deformation. The numerical model uses the VOF methodology in both 2D axisymmetric and 3D computational domains; the latter accounts for the bi-axial droplet motion and deformation, which is usually neglected. The following sections include initially a brief description of the CFD model and the numerical setup, followed by the results and their assessment which aim to shed light into the physical and numerical parameters that affect the model predictions. The conclusions of the present work are summarized at the end.

2 Numerical model and methodology

The numerical model solves the Navier-Stokes equations while the gas-liquid interface is tracked by using the VOF methodology as described recently by the group of authors in (Malgarinos et al., 2015; Malgarinos et al., 2014). To enhance the accuracy of computations with a low computational cost, an automatic local grid

refinement technique is used based on the work of (Theodorakakos and Bergeles, 2004) and implemented as in (Malgarinos et al., 2014). To minimize the diffusion of the interface, an iterative sharpening technique is implemented at the end of each timestep as in (Strotos et al., 2015).

The simulations were performed with the commercial CFD tool ANSYS FLUENT v14.5 (ANSYS®FLUENT, 2012) along with various user defined functions (UDFs) for the implementation of the adaptive local grid refinement, the sharpening technique and the adaptive timestep for the implicit VOF solver mentioned latter in the text. The following "reference" settings have been considered as starting point: Laminar flow, explicit VOF solution with the CICSAM discretization scheme (Ubbink, 1997), moving grid with automatic local grid refinement, Second Order Upwind discretization for the momentum equations (Barth and Jespersen, 1989), PRESTO pressure interpolation scheme (ANSYS®FLUENT, 2012), velocity-pressure coupling with the PISO algorithm (Issa, 1986), variable timestep with Courant number C=0.25 both for the interface tracking and the whole computational domain (global Courant number).

In addition to the explicit VOF solver, the implicit VOF solver was also examined in which the momentum and the volume tracking equations are solved simultaneously in every iteration and much higher timesteps are allowed. The numerical settings adopted for the implicit VOF solver was to use the Compressive discretization scheme for the interface tracking, while for the temporal discretization the Bounded Second Order Implicit formulation was used (ANSYS®FLUENT, 2012). A UDF was implemented in order to achieve a variable timestep by assuming high Courant

numbers (calculated as in (Ubbink, 1997)) in the range C=1-3; the computational cost decreases by almost 1/C. A list of the settings adopted for the two VOF solvers (explicit and implicit) is given in Table 1.

Table 1: List of the numerical settings adopted for the explicit and the implicit VOF solver.

	Explicit	**Implicit**
Temporal discretization	First Order Implicit	Bounded Second Order Implicit
Time-step	Variable (C=0.25)	Variable (C=2.0)
VOF discretization	CICSAM	Compressive
Momentum discretization	Second Order Upwind	Second Order Upwind
pressure interp. scheme	PRESTO or BFW	PRESTO or BFW
velocity-pressure coupling	PISO	PISO

3 Results and discussion

3.1 Cases examined and numerical setup

The model performance was assessed by comparing the numerical results against the experimental data of (Flock et al., 2012) for the bag breakup regime (We=13) and the sheet thinning breakup regime (We=32). (Flock et al., 2012) examined ethyl alcohol droplets (D=2.33mm, Oh=0.0059) injected inside a continuous air jet flow with adjustable velocity leading to different breakup regimes. For the case of bag breakup, the mean air velocity was set equal to 10m/s resulting in We=13 and Re=1500, while for the sheet thinning breakup regime the corresponding values were 16m/s, 32 and 2500 respectively. The droplets were falling from a height of 175mm above the air jet and had a downward velocity approximately equal to 1.85m/s when they approach its area of influence; the experimental configuration of (Flock et al., 2012) is shown in Fig.2a in which the droplet trajectory is denoted with a dashed dotted arrow. The droplet shape, trajectory and dimensions were monitored with the aid of high-speed shadowgraphy (HSS), while Particle Image Velocimetry (PIV) was used to provide information for the gas velocity and streamlines. The experimental measurements include both mean and standard deviation values. Equally important for the predictions, is the fact that the initial and boundary conditions are well defined.

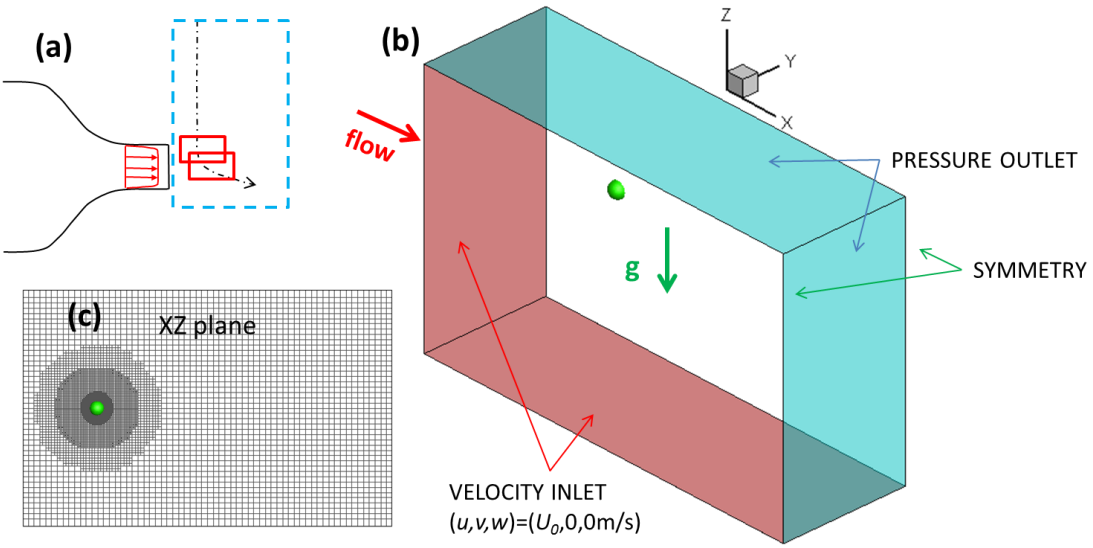

297

298 Fig.2: (a) sketch of the experimental setup of (Flock et al., 2012), (b) computational
299 domain and boundary conditions used for the 3D simulations, (c) computational grid
300 at the symmetry plane.

301

302 Ideally, a large static computational domain (shown as dashed, blue rectangle in
303 Fig.2a) with the appropriate boundary conditions at the region of the nozzle would be
304 required to simulate the experiment. However, the large size of the computational
305 domain would dramatically increase the computational cost, having also in mind that
306 approximately 190ms are required for the free falling droplet to enter inside the air jet;
307 this time interval is rather long when compared to the overall 10-12ms duration (for
308 the *We*=13 case) of the droplet deformation and breakup process that needs to be
309 simulated. So, the strategy adopted in the present work, was to use a small
310 computational domain (solid, red rectangles in Fig.2a) moving with the average
311 droplet velocity vector. The simulations start at the instance when the droplet enters
312 the air jet assuming a step change of the gas phase velocity; the droplet is initially
313 assumed to be spherical with a downward velocity equal to 1.85m/s. The spherical

droplet assumption might affect the predictions as well as the initial droplet perturbation when exiting the orifice might affect the overall droplet deformation; however, as no information regarding these points was provided in (Flock et al., 2012), the effect of these parameters was not examined.

The computational domain along with the boundary conditions used for the 3D simulations is shown in Fig.2b. The boundaries have been placed $16R_0$ far from the droplet in the YZ plane and $40R_0$ far downwind the droplet in order to minimize their effect on the numerical results. In an effort to further reduce the computational cost, only half of the droplet is simulated applying symmetry boundary conditions. Adopting this assumption, results in ignoring possible vortex shedding in the XY plane (which can be expected due to the *Re* number of the flow); however, this assumptions is supported by the relevant experimental data of (Flock et al., 2012), which, judging from the PIV measurements, suggest that the structure of the wake behind the droplet plays rather a minor role. The grid topology in the XZ symmetry plane is shown in Fig.2c. It consists of 2 levels of static local refinement and 4 levels of dynamic local refinement which finally resulted in a grid density of 96cpR at the vicinity of the droplet interface; the static refinement was used to improve the load balance between the nodes used for parallel processing. The total number of cells was 1.1-2.8M depending on the droplet deformation. The computational cost for the explicit VOF solver was approximately 105cpu-days/ms (i.e 35days in 36 nodes to simulate 12ms), while the implicit VOF solver requires significantly lower computational cost (25cpu-days/ms for a global Courant number equal to 2). It has to be noted that the computational cost for a denser grid of 192cpR increases at least by a factor of 7, since the number of the computational cells increases at least by a factor

of 3.5 (based on a spherical droplet) with a timestep decrease by a factor of 2. Nevertheless, the purpose of the 3D simulations is to identify if reasonable predictions can be obtained, even with a relatively coarse grid of 96cpR.

Apart from the computationally expensive 3D simulations, useful information with low computational cost can be obtained by using 2D axisymmetric domains which ignore the vertical droplet motion and the gravitational forces, the vortex shedding behind the droplet and the 3D structures during breakup. The computational grid and the boundary conditions used for the 2D simulations are shown in Fig.3; for reasons of distinctness, the coarse grid with 5 levels of local grid refinement (96cpR) is shown, but simulations were also performed with 6 and 7 levels of local refinement (corresponding to 192 and 384cpR respectively). The lower part of Fig.3 shows the adaption of the grid to the droplet interface (red line corresponding to VOF=0.5), while the inset figures aim to clarify the grid topology near the interface; those grids correspond to the case with We=32.

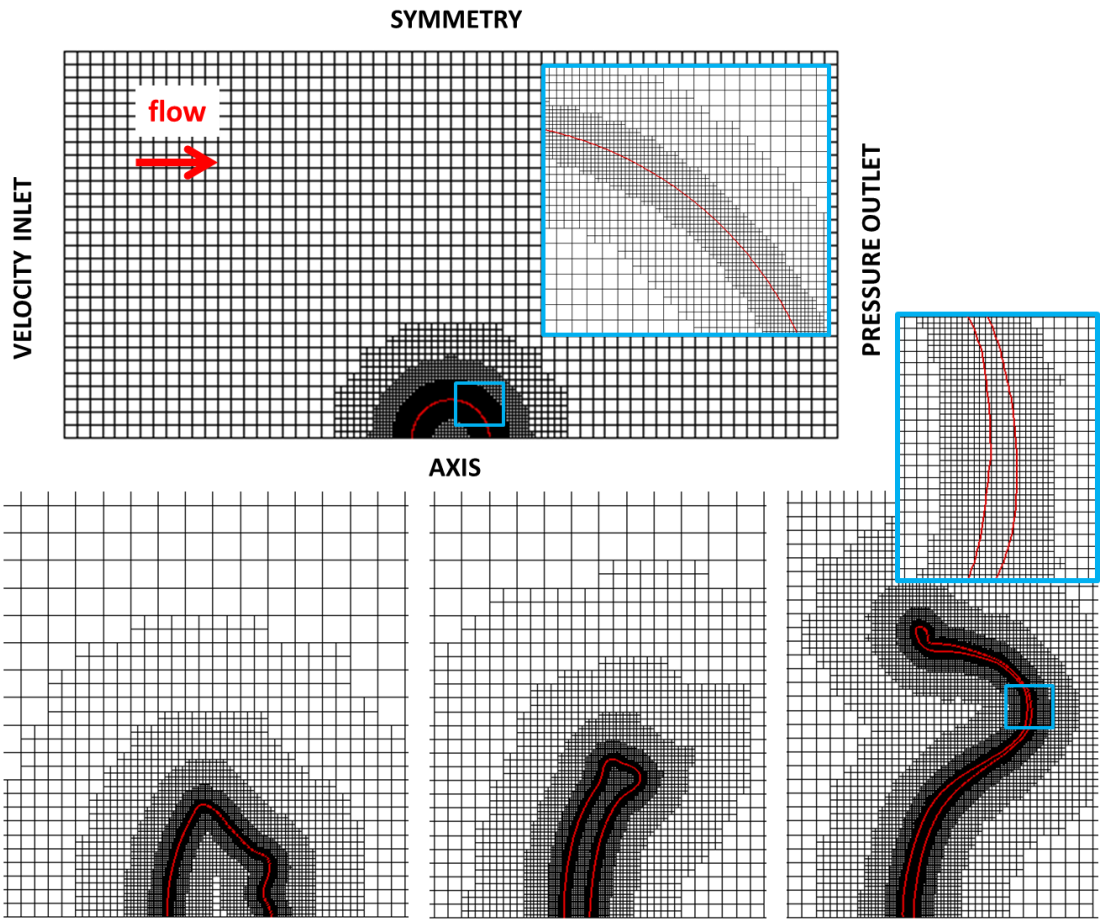

353

354 Fig.3: Computational grid and boundary conditions for the 2D simulations. (5 levels
355 of local grid refinement, 96cpR)

356

357 The 2D simulations were conducted on a computational domain moving with the
358 instantaneous average droplet velocity; the droplet is initially motionless and it is
359 suddenly subjected to a step change of the gas phase velocity. Upstream of the
360 droplet, a fixed absolute velocity equal to 10m/s (or 16m/s) and downstream a fixed
361 pressure profile equal to 1atm have been applied respectively. Note that adopting a
362 moving computational domain with a step change of the gas phase velocity (both for
363 the 2D and 3D simulations), results in ignoring the transitional period in which the

droplet enters the continuous air jet flow; nevertheless this period is quite short and it not expected to affect the model performance. A complete list of the assumptions adopted in the present work is listed in Table 2 for the 2D and the 3D simulations; these arise either from the limited computational resources (for the 3D simulations), or from the nature of the 2D simulations.

Table 2: List of the assumptions adopted for the 2D and the 3D model.

Simplification assumption	**2D**	**3D**	**Expected impact**
Coarse grid		√	high
Ignoring 3D structures	√		high (near breakup)
Ignoring vortex shedding	√	√ (in XZ plane)	medium
Ignoring vertical droplet motion and gravitational forces	√		medium
Initially spherical droplet	√	√	medium
Ignoring droplet motion prior entering the air jet	√	√	low
Step change of gas phase velocity	√	√	low

The results obtained with the 2D axisymmetric model are presented in section 3.2, while the more representative of the real conditions 3D results are presented in section 3.3. In section 3.4 a parametric study for a wider range of *We* numbers is performed and an overall discussion of the results obtained with these approaches is performed in section 3.5. A list of the cases examined is given in Table 3.

380 Table 3: List of the cases examined.

	2D	3D
We=13 (bag)	EXPL/IMPL, PRESTO/BFW	EXPL/IMPL, PRESTO/BFW
We=32 (sheet)	EXPL/IMPL, PRESTO/BFW	EXPL/IMPL, PRESTO/BFW
We=15-90 (parametric)	EXPL, PRESTO	

381

382

383 ## 3.2 2D simulations

384 The results of the present 2D model for the bag breakup case (*We*=13) are presented
385 in Fig.4 for three different grid sizes namely 96, 192 and 384cpR. On the left-hand-
386 side of the figure, the predicted dimensionless droplet dimensions in the stream-wise
387 direction x and the cross-stream direction y (denoted with solid lines which turn into
388 dashed after the droplet breakup) are compared against those reported by (Flock et al.,
389 2012); error bars for the standard deviation of the measurements are also given, while
390 the experimental time has been shifted by 1ms since the experimental time *t*=0
391 corresponds to a slightly deformed droplet. On the right-hand-side of Fig.4 typical
392 droplet shapes are shown, assuming the VOF=0.5 to represent the droplet interface
393 and at the lower part of Fig.4 a three-dimensional representation of the breakup

process is shown; this was obtained by revolving the 0.5 VOF iso-value around the symmetry axis. The differences for the droplet shape can be regarded as grid independent during the flattening phase (t<7ms), while slight deviations are observed during the subsequent phase of bag creation. Increasing the grid resolution results in the formation of a thinner bag and shifting of the breakup point away from the axis of symmetry. Nevertheless, the solution can be regarded as grid independent for values higher than 192cpR, but also the 96cpR grid could be used to provide useful information on droplet breakup with a lower computational cost (this was increased by a factor of 2.75 when the grid resolution was doubled). On the other hand, the exact droplet dimensions reported in the experiment of (Flock et al., 2012) could not be captured with the axisymmetric approach, but the droplet breakup and the general trend of the evolution of the droplet shape are in accordance with the experimental observations. It seems that using an even denser grid than the one with 384cpR, would not improve the performance of the 2D model. This is attributed to the inevitable simplifications characterizing the 2D axisymmetric model. It has also to be noted that the results of the 2D axisymmetric model are not affected by the adopted numerical settings (i.e. discretization schemes and pressure interpolations schemes) as it was shown in (Strotos et al., 2015).

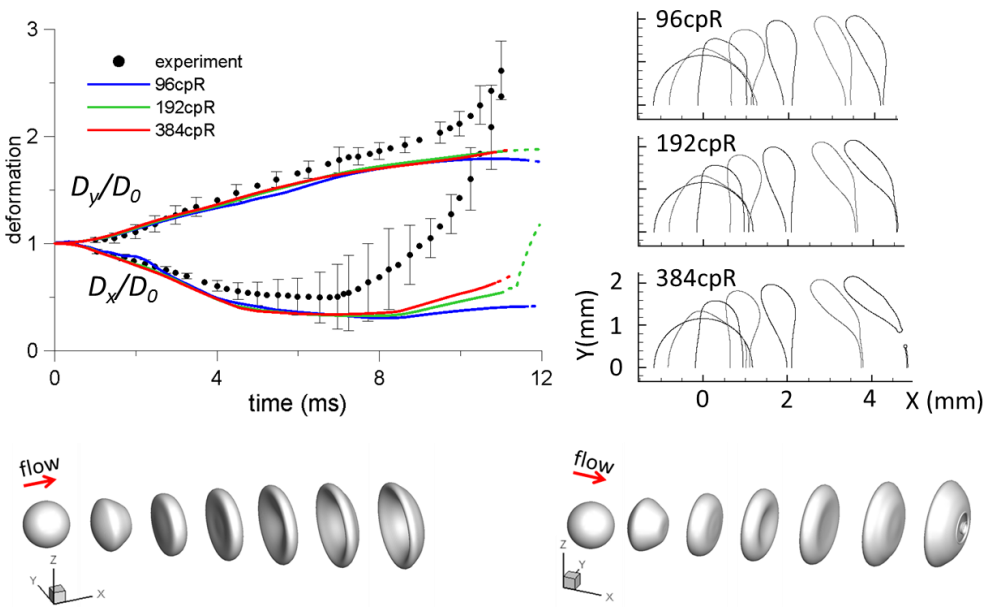

413

414 Fig.4: Temporal evolution of the droplet dimensions and droplet shapes (in intervals
415 of 2ms) for three different grid densities (*We*=13, 2D axisymmetric domain). The last
416 droplet shape corresponds to 11ms which is approximately the time of breakup. The
417 bottom row shows a three-dimensional representation of the droplet shapes by
418 revolving the 0.5 VOF iso-value.

419

420 In an effort to speed-up the calculations, the implicit VOF solver was also examined,
421 which allows for much higher time-steps without the Courant number restriction of
422 the explicit methodology. Variable time step was used through a user defined
423 function; the global Courant number was kept constant, but much higher (values up to
424 *C*=3 were examined) compared to the 0.25 value used in the explicit solver. The
425 performance of the implicit solver for three different Courant numbers is shown in
426 Fig.5 for the case of bag breakup with 192cpR grid. As it can be seen, it is
427 encouraging that the global Courant number can be increased up to 3.0 with the

numerical accuracy remaining almost the same; some differences are observed only after the breakup.

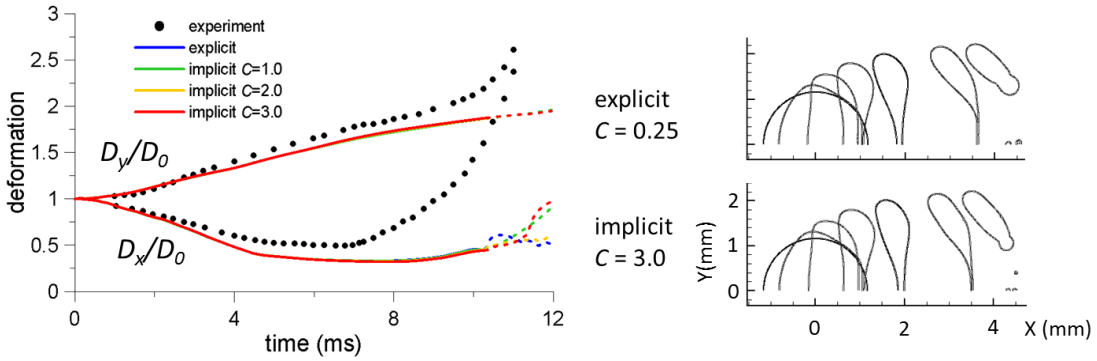

Fig.5: Effect of implicit VOF solution in the 2D predictions of the bag breakup case (*We*=13) with the Compressive VOF discretization scheme and the sharpening algorithm.

The results of the 2D axisymmetric model for the sheet thinning breakup (*We*=32) are presented in Fig.6 for three different grid densities (96, 192 and 384cpR). As in the bag breakup case, the droplet deformation for the flattening phase (t<3ms) is in accordance with the experimental observations and measurements and it is not affected by the grid density. After the initial flattening phase, the solution becomes grid independent for 192cpR. But even in this case, the cross-stream deformation D_y/D_0 is over-predicted and more importantly, the droplet shape corresponds to rather a transitional regime than the sheet-thinning breakup shown in the experimental photos of (Flock et al., 2012). This transitional regime is characterized by a toroidal bag formed at the droplet periphery which eventually breaks up and it is something between the dual-bag and the plume/shear breakup regimes mentioned in the

446 introduction; these regimes are observed for 30<*We*<80 (see Fig.1b). This point will
447 be further analyzed in section 3.5.

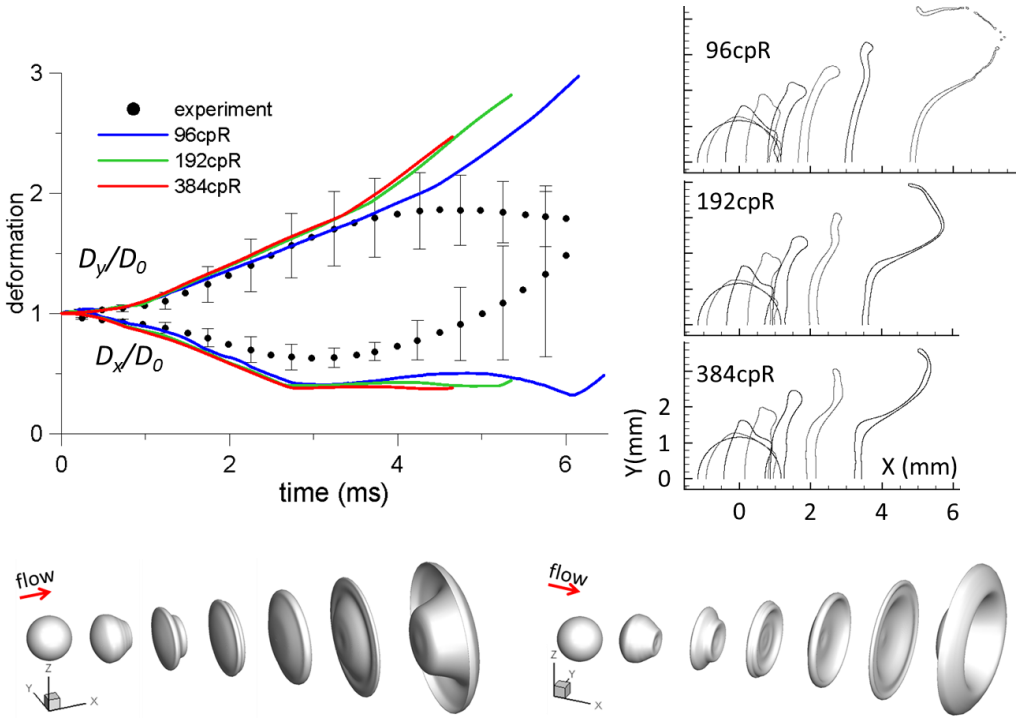

448

449 Fig.6: Temporal evolution of droplet dimensions and droplet shape evolution in 1ms
450 intervals for three different grid densities (*We*=32, 2D axisymmetric domain). The
451 bottom row shows a three-dimensional representation of the droplet shapes by
452 revolving the 0.5 VOF iso-value.

453

454 ## 3.3 3D simulations

455 In this section, the results obtained with the 3D model will be presented in two
456 separate sub-sections for the bag breakup case (section 3.3.1) and the sheet-thinning
457 breakup case (section 3.3.2). In contrast to the 2D axisymmetric model which had a
458 robust behavior, the 3D model performance is greatly affected by the pressure
459 interpolation scheme. For that reason, the following sections include results from both

460 the PRESTO and the Body Force Weighted (BFW) pressure interpolation schemes, as
461 also results obtained with the implicit VOF solver which speeds-up the calculations
462 by allowing higher computational time-steps.

463

464 ### 3.3.1 Bag breakup (*We*=13)

465 The predictions of the 3D CFD model for the droplet dimensions and the droplet
466 trajectory are shown in Fig.7 for the case of bag breakup (*We*=13). The numerical
467 settings examined are the following: (I) explicit VOF solution with either the
468 PRESTO or the BFW pressure interpolation scheme and (II) the implicit VOF
469 solution with the BFW scheme assuming a global Courant number equal to 2. The
470 flattening phase in Fig.7a is generally correctly predicted and at the bag creation
471 phase the model under-predicts the droplet deformation along the cross-stream
472 direction (z) with a lower rate of deformation in the stream-wise direction (x).
473 Examining also the predictions for the droplet trajectory (Fig.7b) it seems that the
474 explicit VOF solution with BFW pressure scheme is rather the best approach.

475

476

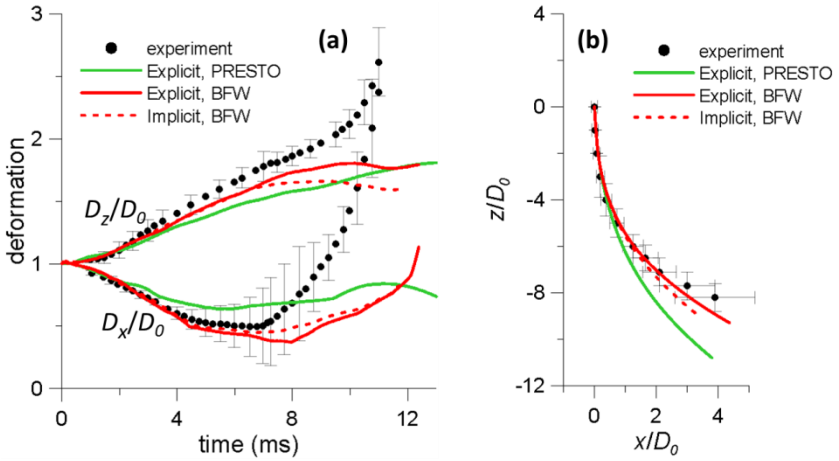

477

478 Fig.7: Predictions of the 3D model for the bag breakup case (*We*=13) for the droplet
479 dimensions (a) and the droplet trajectory (b).

480

481 In contrast to the 2D simulations, the pressure interpolation scheme seems to play an
482 important role in the 3D simulations. As a matter of fact, the PRESTO scheme
483 exhibits higher deviation from the experimental data and it is not leading to droplet
484 breakup. This is clearly shown in Fig.8 in which the droplet shapes in intervals of 2ms
485 are shown. The shapes on the top row are projections of the droplet interface (xz
486 plane) in the stream-wise direction, while the bottom row shows the actual droplet
487 shape and position. From the top row it is evident that the PRESTO scheme does not
488 predict breakup, while the BFW scheme (both in explicit and in implicit solution)
489 predicts correctly the flattening (*t*=0-6ms), the bag creation (*t*=8-10ms) and the
490 breakup (*t*=12ms). A more detailed presentation of the droplet shapes is shown in
491 Fig.9 for the case of explicit VOF solution with the BFW scheme. The droplet
492 deformation is presented from three different viewpoints and the characteristic phases
493 of the bag breakup are clearly shown.

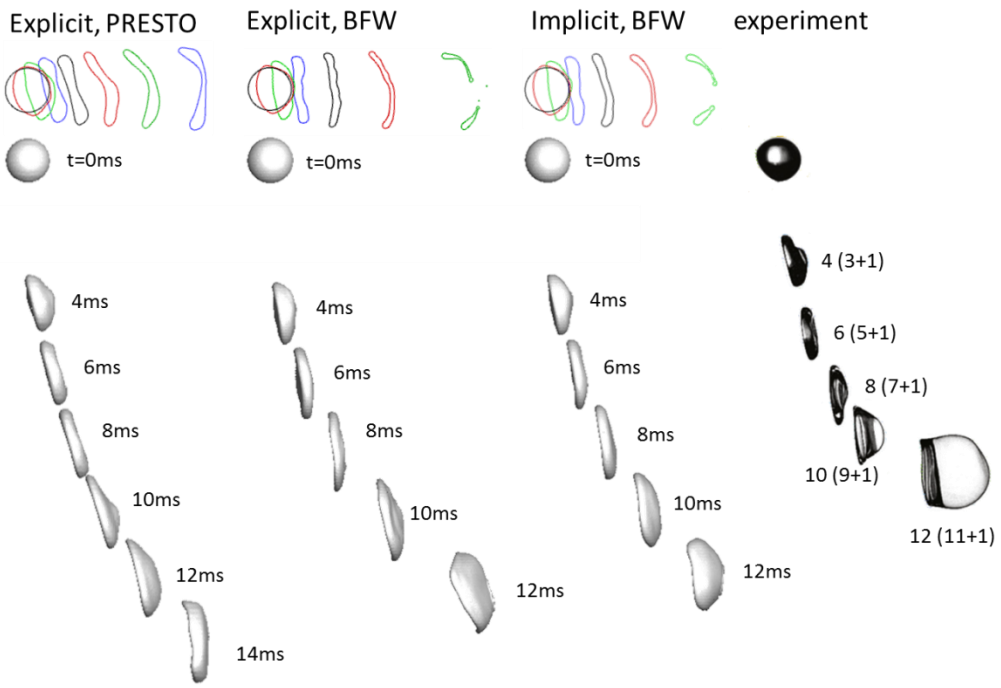

494

495 Fig.8: Predictions of the 3D model for the bag breakup case (*We*=13) for the droplet
496 shape and trajectory (in intervals of 2ms). At the right part, the experimental photos of
497 (Flock et al., 2012) corresponding to Figure 10 of their paper, are also shown; their
498 experimental time has been shifted by 1ms.

499

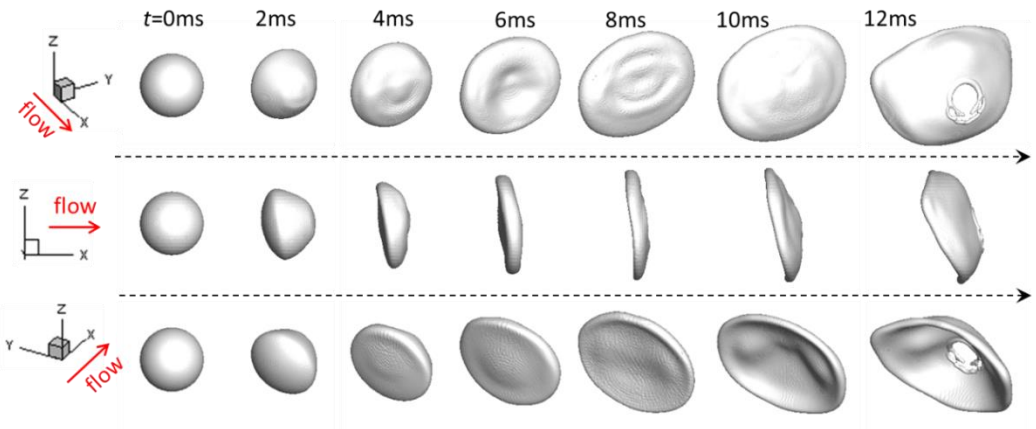

500

501 Fig.9: Different views of the droplet shape for the bag breakup case (*We*=13) in
502 intervals of 2ms for the case of explicit VOF solution with the BFW scheme.

503

Focusing on the differences between the two pressure interpolation schemes, it is interesting to examine the predicted flow field. This is shown in Fig.10 and Fig.11 for the PRESTO and the BFW pressure interpolation schemes respectively. The 1st row of the figures shows the pressure field, the 2nd row the absolute velocity streamlines and the 3rd row the relative velocity streamlines; the latter are coloured with the corresponding velocity magnitude and the relative velocity is obtained by subtracting the velocity of the droplet from the velocity vector. Regarding the pressure field, in both cases a high pressure region appears in the front stagnation point, while at the rear side of the droplet low pressure regions appear at the vortex cores. Regarding the velocity field (either absolute or relative), the differences between the two pressure schemes are important. The PRESTO scheme predicts a quite smooth velocity field with large vortical structures, which closely resembles the average velocity field identified with the PIV technique in (Flock et al., 2012) (see Fig.12a). On the other hand, the BFW scheme exhibits a relatively disturbed velocity field with smaller and more chaotic vortices; similar eddies were identified in (Flock et al., 2012) in the instantaneous (and not the averaged) velocity field (see Fig.12b). Note also that the BFW scheme predicts vortex shedding, while the PRESTO scheme does not. Vortex shedding is expected in this case (Re=1500) since it is observed for Re numbers in the range 400-$3\cdot10^5$. In (Flock et al., 2012) for the same conditions they identified symmetrical vortices for some cases and alternating vortices for some other; it was concluded that this point requires further experimental evidence.

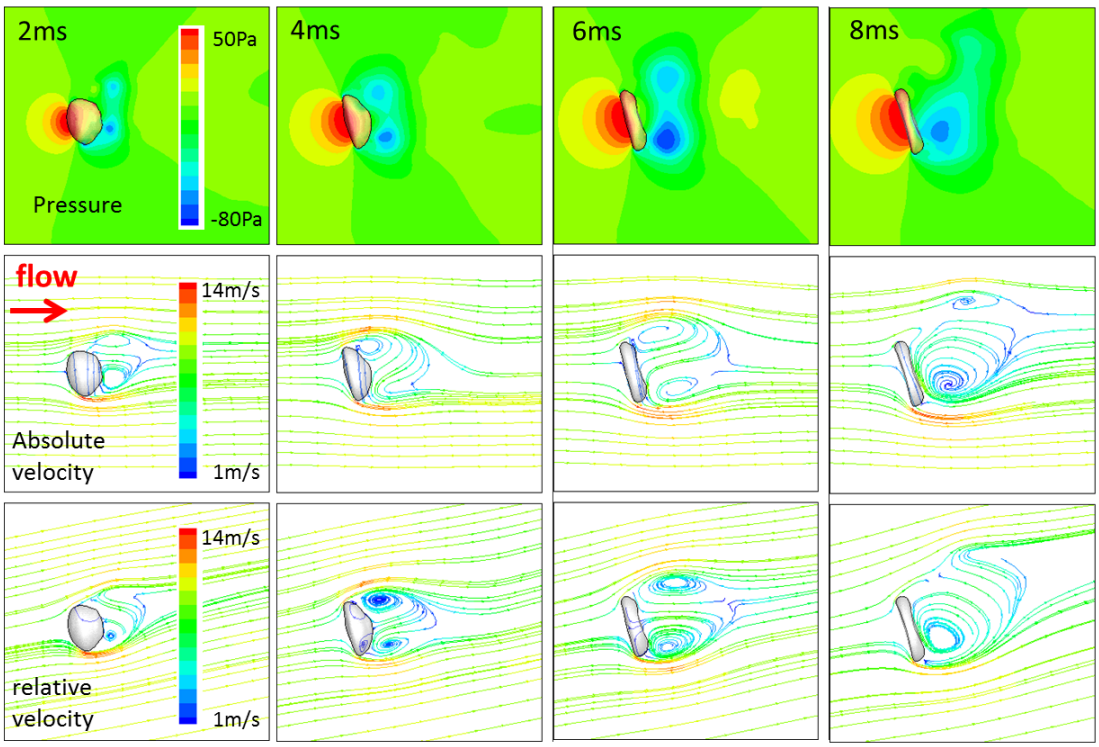

526

527 Fig.10: Predicted pressure and velocity field for the bag breakup case (*We*=13) using
528 the PRESTO scheme.

529

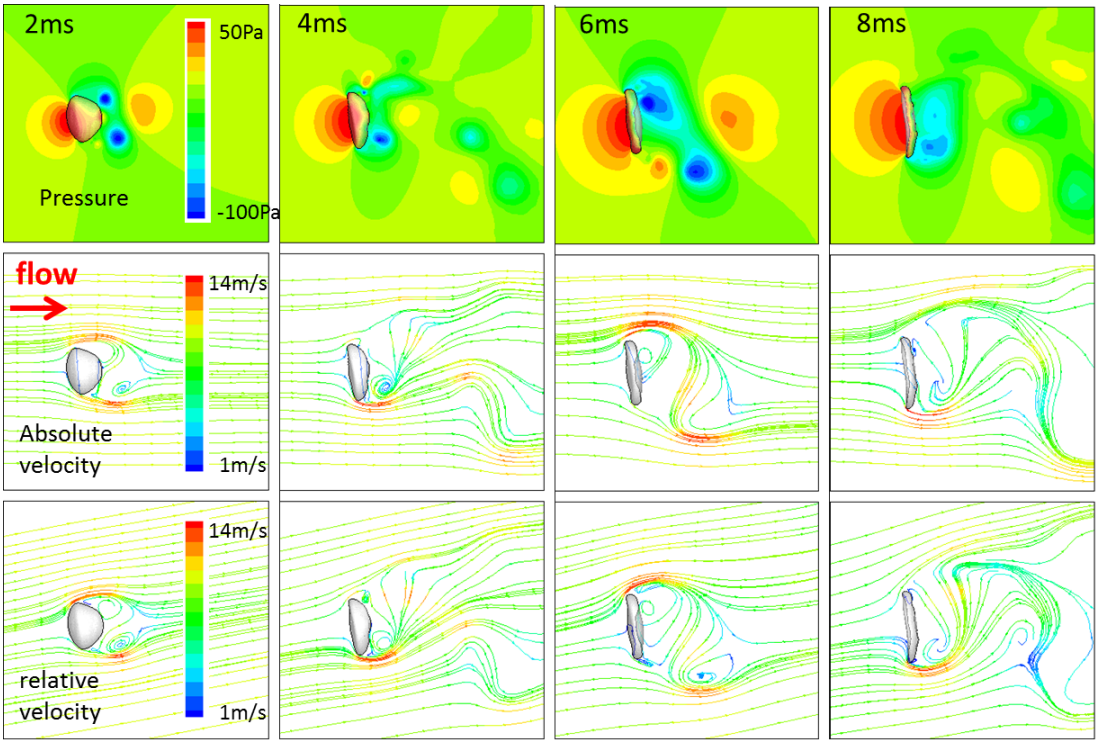

530

531 Fig.11: Predicted pressure and velocity field for the bag breakup case (*We*=13) using
532 the BFW scheme.

533

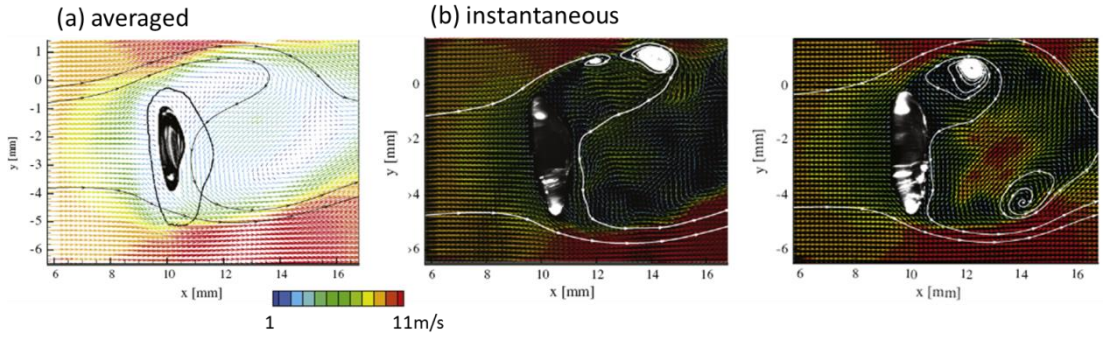

534

535 Fig.12: (a) Averaged and (b) instantaneous velocity field at 7ms obtained with the
536 PIV technique in (Flock et al., 2012) for the bag breakup case (*We*=13).

537

3.3.2 Sheet thinning breakup (*We*=32)

The predictions for the droplet dimensions and the droplet trajectory for the sheet thinning breakup case (*We*=32) are shown in Fig.13. The numerical settings examined are the combinations of two solution algorithms (explicit with the CICSAM discretization scheme and implicit with the Compressive scheme) and two pressure interpolation schemes (PRESTO and BFW). The case with the implicit solution and PRESTO scheme exhibited unphysical disturbances in the interphase and was re-examined with a lower global Courant number equal to 1.5. In Fig.13a the flattening phase (t<3ms) is more or less similar for the two pressure schemes with some differences after t=2ms in which the BFW scheme predicts slightly higher deformation. Both schemes predict the same trend with the experimental measurements; nevertheless they both predict higher deformation in the stream-wise direction x compared to the experimental data. In the subsequent phase of sheet creation (t>3ms) the differences between the two pressure interpolation schemes are more distinct; the PRESTO scheme exhibits higher rate of deformation compared to the experimental data, while the BFW scheme predicts correctly the deformation rate but the whole curve is shifted below the experimental one for the cross-stream deformation due to the higher deformation predicted at the end of the flattening phase (t~3ms). At the stages near the sheet breakup (t>4.5ms), both schemes predict increasing deformation in the z-direction (with a slightly better behaviour for the BFW scheme) which contradicts the experimental data. On the other hand, similar trends in increasing deformation were observed in the experimental works of (Cao et al., 2007; Jain et al., 2015; Zhao et al., 2013), while the over-estimation of the cross-stream diameter was also present in the detailed simulations of (Jain et al., 2015) for

562 *We*=40 and 80. The discrepancies of the present predictions relative to the
563 experimental data will be further discussed in section 3.5. Regarding the droplet
564 trajectory in Fig.13b, all cases examined predict the same droplet motion which
565 exhibits a higher velocity in the z-direction compared to the experimental one. On the
566 other hand, the predictions for the droplet trajectory refer to the position of the mass
567 centre, which is different from the geometric centre obtained from the outer contour
568 of the drop shadow in (Flock et al., 2012) and does not account for the distribution of
569 mass in the liquid structure. This fact can explain the differences between predictions
570 and measurements in Fig.13b.

571

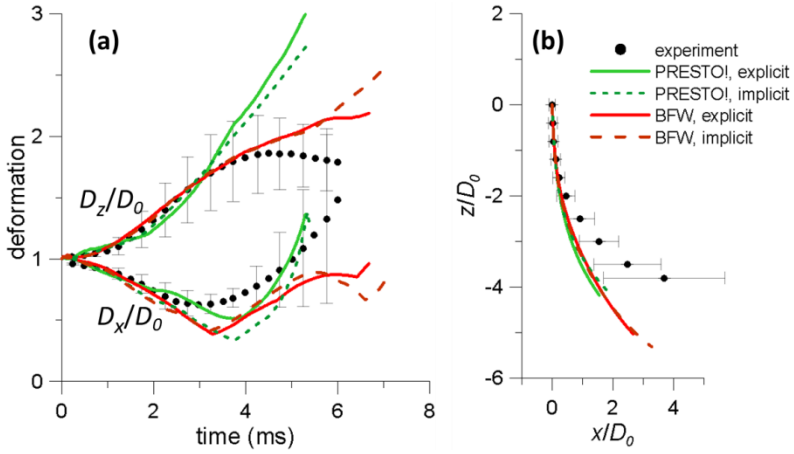

572

573 Fig.13: Predictions of the 3D model for the sheet thinning breakup case (*We*=32) for
574 the droplet dimensions (a) and the droplet trajectory (b).

575

576 The side view of the predicted droplet shapes in 1ms time intervals for the four cases
577 examined are shown in Fig.14 and detailed information on the droplet shapes from 3
578 different viewpoints are shown in Fig.15 and Fig.16 for the PRESTO and BFW

schemes respectively (explicit VOF solver). All cases examined are finally leading to breakup but a slightly different behaviour is observed between the PRESTO and the BFW scheme after the flattening phase (t=3ms). The PRESTO scheme predicts the formation of a sheet at the droplet periphery in the stream-wise direction while its leading edge bends and forms a disc (similar droplet shapes where obtained with the 2D axisymmetric model); the droplet deformation is not axisymmetric (see Fig.15) and this is attributed to interfacial instabilities, but also due to the symmetry boundary condition which allows for vortex shedding only in the xz plane. The bend in the leading edge is also present in the experimental photos of (Flock et al., 2012) but seems to be more intense at the lower part of the droplet. Finally the sheet breaks up at the junction of the stream-wise sheet and the leading edge. This breakup regime can be regarded as the plume/shear regime. On the other hand, the BFW scheme predicts a slightly different kind of deformation. The sheet formed is not changing curvature at its leading edge and at t=6ms the droplet deformation turns into a shape resembling the bag-and-stamen regime; more details on the droplet shapes can be seen in Fig.16. The accuracy of the predictions with the BFW scheme will be further discussed in section 3.5.

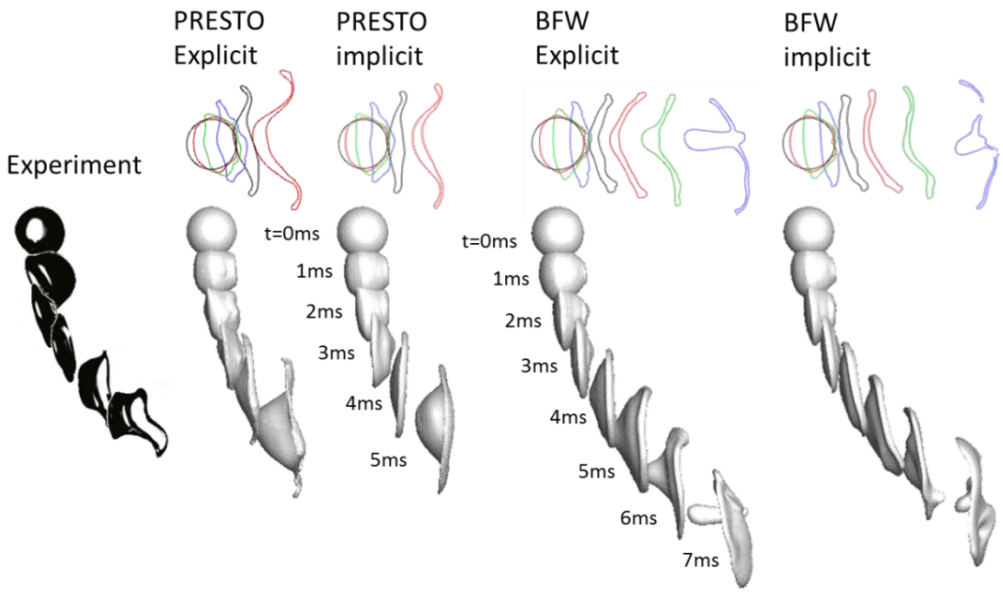

597

598 Fig.14: Predictions of the 3D model for the sheet thinning breakup case (*We*=32) for
599 the droplet shape and trajectory (in intervals of 1ms). At the left part, the experimental
600 photos of (Flock et al., 2012) corresponding to Figure 15 of their paper, are also
601 shown.

602

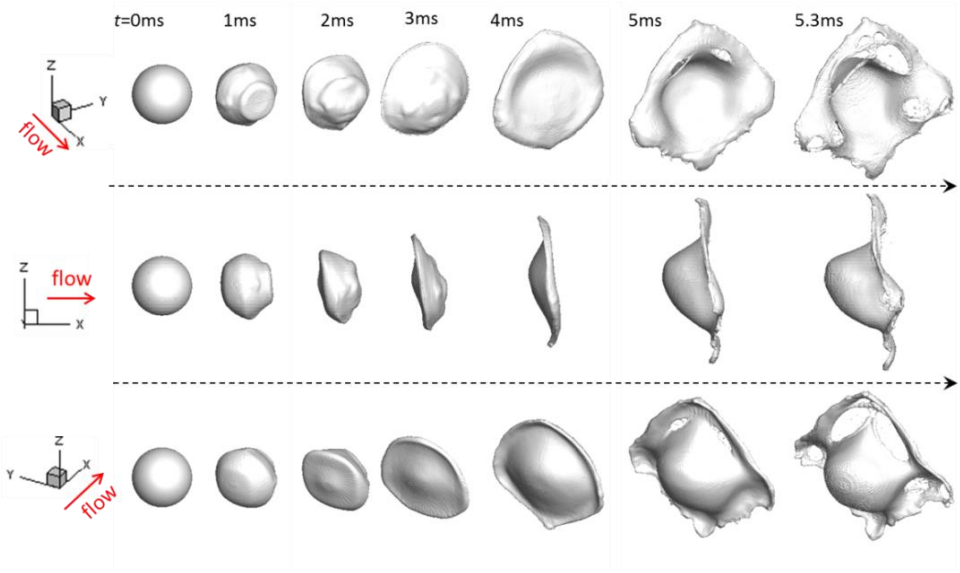

603

604 Fig.15: Different views of the droplet shape in intervals of 1ms for the case of explicit
605 VOF solution with the PRESTO scheme for the sheet thinning breakup case (*We*=32).

606

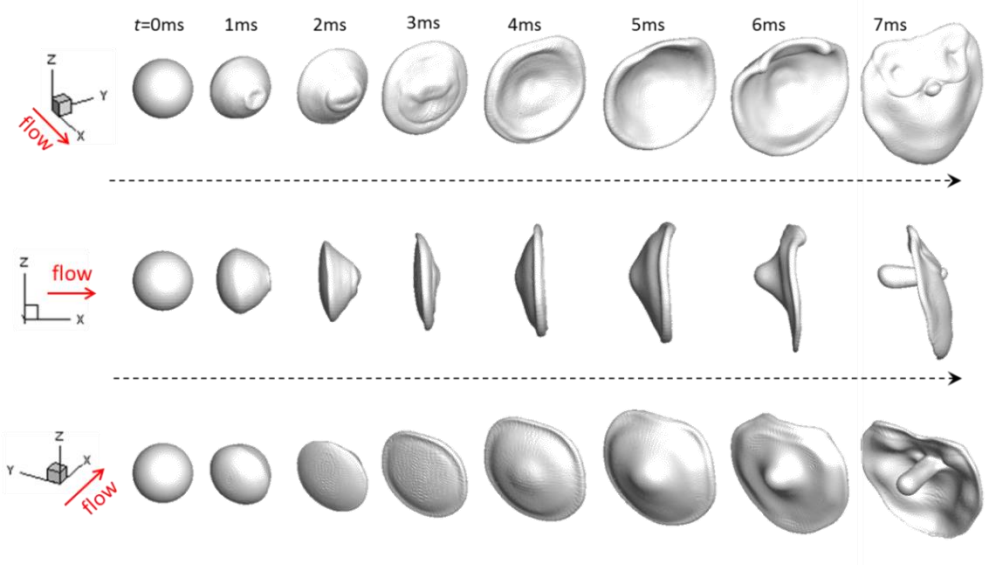

607

608 Fig.16: Different views of the droplet shape in intervals of 1ms for the case of explicit
609 VOF solution with the BFW scheme for the sheet thinning breakup case (*We*=32).

610

611 Regarding the predicted velocity field for the two pressure interpolation schemes, the
612 comments made for the bag breakup case in section 3.3.1, apply also for the sheet
613 thinning breakup case. The PRESTO scheme (Fig.17a) exhibits a rather steady-state
614 velocity field similar to the averaged one presented in (Flock et al., 2012) (see
615 Fig.18a), while the BFW scheme (Fig.17b) predicts a transient velocity field with
616 vortex shedding which is closer to the instantaneous velocity field presented in (Flock
617 et al., 2012) (see Fig.18b); this was rather expected due to the *Re* number of the flow
618 (*Re*=2500), but as stated in (Flock et al., 2012) this point requires more experimental
619 evidence.

620

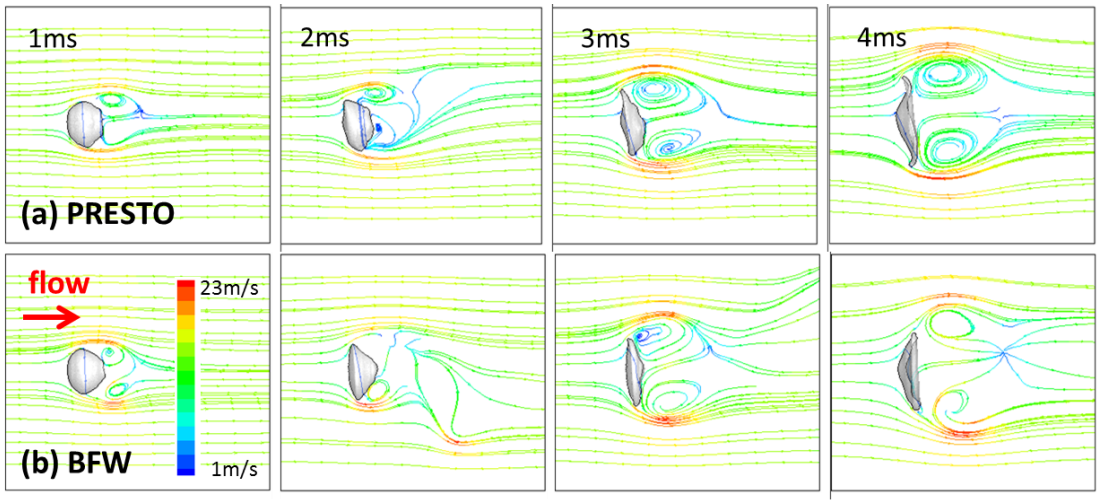

Fig.17: Predicted absolute velocity field for the sheet thinning breakup case (*We*=32) using explicit VOF for (a) the PRESTO and (b) the BFW scheme.

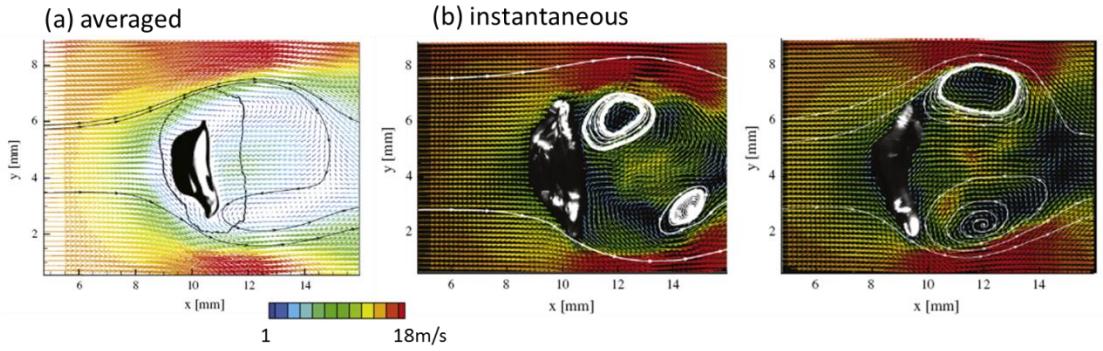

Fig.18: Averaged (a) and instantaneous (b) velocity field at 4ms obtained with the PIV technique in (Flock et al., 2012) for the sheet thinning breakup case (*We*=32).

3.4 Parametric study

In an effort to further explore the model capabilities in predicting the various breakup regimes, a parametric study has been performed by examining well established *We* numbers which lead to the different breakup regimes presented in Fig.1. This time the

633 model performance will be assessed based on qualitative criteria without a direct
634 comparison with specific experimental data; this is a common practice to validate
635 CFD models and it was used by the majority of the studies mentioned in the
636 introduction. The conditions examined are those of (Flock et al., 2012), i.e. 2.33mm
637 ethyl alcohol droplets in air, but with a varying gas phase velocity leading to *We*
638 numbers 15, 20, 40 and 100 which correspond to bag, bag-stamen, transition
639 (plume/shear) and sheet-thinning breakup respectively. The simulations were
640 performed with the explicit VOF solver, CICSAM and PRESTO schemes, 192cpR
641 grid in a 2D axisymmetric domain which ignores the vortex shedding behind the
642 droplet, but as it will be seen, this is not affecting the breakup outcome. The results
643 obtained for the droplet shapes are presented in Fig.19a for time intervals of $0.05\tau_{sh}$. It
644 is clear that the model can adequately capture the various breakup regimes. For the
645 bag-stamen case (*We*=20), a relatively short stamen is predicted (similar to (Xiao,
646 2012)), while for the sheet-thinning breakup (*We*=100) one can see the interfacial
647 instabilities at the initial stages and the continuous stripping from the droplet
648 periphery during breakup; similar instabilities (Kelvin-Helmholtz and Rayleigh-
649 Taylor instabilities) were also identified in the numerical work of (Jalaal and
650 Mehravaran, 2014). In Fig.19b,c the predicted (up to the breakup instant) droplet
651 deformation and droplet velocity are presented along with the experimental data of
652 (Dai and Faeth, 2001) for $20<We<81$; these have been digitized and further processed
653 in order to be presented in the axes shown in Fig.19b,c. As seen, the model results
654 agree with the experimental measurements. Increasing the *We* number results in
655 increasing the rate of deformation as also earlier breakup which is in accordance with
656 the experimental findings of (Pilch and Erdman, 1987) and (Dai and Faeth, 2001).

The droplet velocity (normalized with the instantaneous drop-gas relative velocity $U_0 - u$), increases with time without a noticeable effect of We number and it is in accordance with the experimental data.

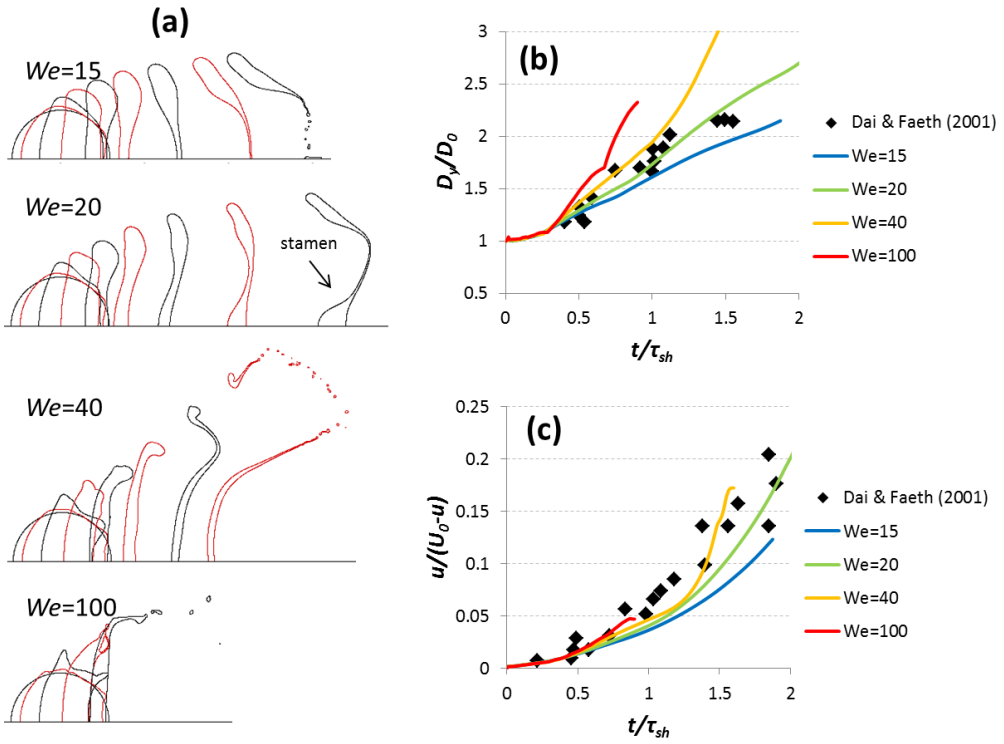

Fig.19: Parametric study for the effect of *We* number (2D axisymmetric simulations). (a) Droplet shapes corresponding to time intervals of $0.05\tau_{sh}$, (b) cross-stream droplet deformation, (c) droplet velocity.

3.5 Discussion

The 3D simulations presented in section 3.3 have shown that the pressure interpolation scheme (PRESTO or BFW) plays an important role, in contrast to the 2D simulations which are generally insensitive on the numerical settings. The BFW

treats the gravitational and surface tension forces similar to the pressure forces; the key assumption is the constant normal gradient to the face of the body force and pressure. According to the authors, this scheme probably acts as a modified Rhie-Chow algorithm (see for example (Gu, 1991) among many other pressure-correction algorithms). This is expected to result to a better balance of the pressure and body forces at the cell face, and thus, to a more accurate solution. The PRESTO scheme is based on the classical staggered grid scheme approach as highlighted by (Patankar, 1980). It uses the explicit discrete continuity balance on a staggered control volume around the face to compute the pressure. From the results obtained for the specific cases simulated here, the main difference between the two schemes is found on the predicted recirculation zones of the 3D cases, which, according to (Yang et al., 2016), these can play a role during droplet breakup. The PRESTO scheme predicts a steady state velocity field without vortex shedding, while the BFW scheme predicts an unsteady velocity field with vortex shedding; this was expected since the *Re* number of the cases examined is above 1500. Having also in mind that the PRESTO scheme cannot predict the bag breakup, it has been concluded the BFW scheme better predicts droplet breakup.

For the bag breakup case, both the 2D axisymmetric (up to the break-up time) and the 3D simulations are in accordance with the experimental observations, predicting quite accurately the flattening phase and having some discrepancies in the bag creation phase for which the bag dimensions are under-predicted. The 2D model which ignores the forces in the vertical direction (including the gravitational one) is not able to capture the secondary droplet deformation and its deviation from the axisymmetric shape (see the experimental photos in Fig.8 and Fig.14). As these forces acting on the

vertical direction, they serve as an inception point and they further promote the creation of the bag; ignoring them results in higher deviation from the experimental dimensions at the latter stages of deformation (see section 3.2) compared to the 3D predictions. On the other hand, the *We* number based on the downward droplet velocity at the instance that the droplet enters the jet is 0.44 and it is two orders of magnitude lower compared to the one based on the jet velocity. For that reason, the influence of the downward motion is not expected to alter the general breakup outcome until the break-up time; that justifies the applicability of the 2D axisymmetric model for the prediction of the initial droplet deformation and break-up time. Moreover, the Froude number based on its classical definition ($Fr=U^2/gD$) is 4374 and 11200 for the two cases examined; a modified Froude number, expressing the ratio of air inertia forces over gravitational forces and defined as $\rho_g U^2/\rho_{liq} gD$, is 6.82 and 17.46 for the two cases, respectively; as the resulting values are much higher than unity, it can be expected that the gravitational forces play a minor role on the breakup process.

Regarding the 3D simulations of the bag breakup case, the discrepancies from the experimental data are attributed to the simplifications made to reduce the computational cost, i.e the adoption of a moving computational domain, the simulation of the half of the droplet, the assumption of initially spherical droplet and the usage of a relatively coarse grid (96cpR); nevertheless, we cannot a-priori estimate the influence of those parameters without performing the corresponding simulations. Another parameter that might affect the model performance is turbulence. The *Re* number based on the nozzle diameter is 17100 and (Flock et al., 2012) report a turbulent intensity of 1.5%. These conditions correspond rather to a

718 transitional flow than a fully turbulent and a 3D LES model (Large Eddy Simulation)
719 should be able to capture the flow structures, but the computational cost would further
720 increase, since a dense isotropic grid would be required in the whole computational
721 domain (not only near the interface) as also a lower Courant number ($\sim$0.2). In
722 (Strotos et al., 2015) it was shown that the RANS turbulence modelling failed to
723 predict the bag breakup, which is accordance with the findings of (Tavangar et al.,
724 2014); on the contrary, LES model was able to capture the phenomenon. Since
725 (Tavangar et al., 2014) used the same grid for both models, this reflects the
726 superiority of LES.

727 Turning now our interest to the sheet thinning breakup case, there is a qualitative
728 agreement between the 2D axisymmetric simulations and the 3D simulations with the
729 PRESTO interpolation scheme, probably due to the steady-state velocity field
730 predicted with these settings. Nevertheless, instead of the sheet thinning breakup
731 shown in the experimental photos, they both predict a plume/shear breakup. A similar
732 contradiction exists also for the 3D predictions with BFW scheme which predicts
733 something between a bag-and-stamen and a dual-bag breakup. On the other hand,
734 similar droplet shapes with the present predictions (see Fig.20a and b) were observed
735 in (Cao et al., 2007; Zhao et al., 2013) for large water droplets at *We*=29 representing
736 the so-called dual-bag breakup. As stated in the introduction, a variety of critical *We*
737 numbers leading to sheet-thinning breakup has been reported in literature. From figure
738 Fig.1 it seems that the *We* number of 32 examined corresponds rather to a transitional
739 regime than a sheet-thinning breakup which is generally observed at higher *We*
740 numbers above 80; nevertheless the critical *We* number might by affected by several

741 other parameters. It seems that the *We*=32 case is in the limit between different
742 breakup modes and such conditions are generally difficult to be captured by CFD
743 codes. This fact in addition to the assumptions made to reduce the computational cost
744 may explain the different breakup regime predicted. Summarizing, the discrepancies
745 observed relative to the experimental measurements are attributed to the assumptions
746 made to minimize the computational cost, while the deviation in the predicted droplet
747 shape for the higher *We* number case is ought to the complicated nature of droplet
748 breakup in the range *We*=20-80, which has been reported in several past works.

749

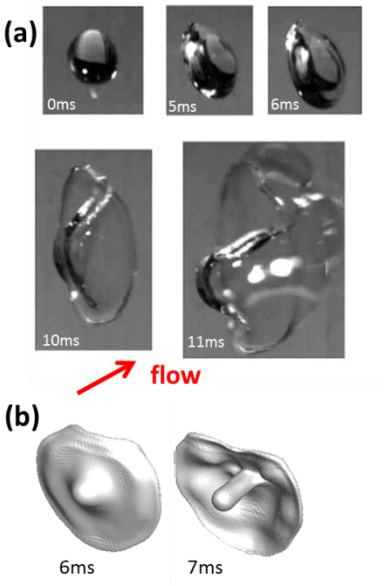

750

751 Fig.20: (a) experimental photos of (Zhao et al., 2013) for the dual-bag breakup of
752 water droplets for *We*=29, (b) present 3D predictions for *We*=32 with the BFW
753 pressure scheme.

754

4 Conclusions

In the present work, the bag breakup and the sheet thinning breakup of droplets subjected to a continuous air flow were studied with the VOF methodology in 2D axisymmetric and 3D computational domains. The model results were compared against experimental data showing a qualitative agreement while the discrepancies observed were attributed to the simplifications made to reduce the computational cost. In addition to that, a parametric study for a wider range of *We* numbers has shown that the model can adequately predict a broad range of breakup regimes.

Whilst the 2D axisymmetric model had a robust behavior and it was not affected by the numerical settings used for the two breakup modes examined, the 3D model was greatly affected by the pressure interpolation scheme which may result in quite different flow types, namely steady-state flow for the PRESTO scheme and transient flow with vortex shedding for the Body Force Weighted (BFW) scheme. Furthermore, the PRESTO scheme was not able to capture the 3D bag breakup case, while in the higher *We* number case both schemes predicted breakup. To the authors' opinion, the BFW scheme (either in the explicit or the implicit VOF solution) is the best choice for 3D calculations. It predicts breakup for both cases examined, despite the fact that for the case with the higher *We* number a bag-stamen breakup was predicted instead of the experimentally observed sheet thinning breakup; in fact this *We* number is rather in the transitional range between different breakup modes and it is not purely representing a sheet thinning breakup. Finally, the implicit VOF solution with variable timestep can provide accurate results with a lower computational cost;

nevertheless unphysical interfacial instabilities were observed for the high *We* case with the 3D PRESTO scheme which were vanished by reducing the Courant number.

5 Acknowledgements

The research leading to these results has received funding from the People Programme (Marie Curie Actions) of the European Union's Seventh Framework Programme FP7-PEOPLE-2012-IEF under REA grant Agreement No. 329116.

6 Nomenclature

Roman symbols

Symbol	Description	Units
C	Courant number $C = u \cdot \delta t/\delta x$	-
D	diameter	m
g	gravitational acceleration	m/s^2
Oh	Ohnesorge number $Oh = \mu_l/\sqrt{\rho_l \sigma D_0}$	-
p	pressure	Pa
R	radius	m
Re	Reynolds number $Re = \rho_g U_{rel,0} D_0/\mu_g$	-
t	time	s
U	reference velocity	m/s
u,v,w	velocity components	m/s
We	Weber number $We = \rho_g U_{rel,0}^2 D_0/\sigma$	-

Greek symbols

Symbol	Description	Units
δt	timestep	s
δx	cell size	m
ε	density ratio $\varepsilon = \rho_l/\rho_g$	-
μ	viscosity	kg/ms
N	Viscosity ratio $N = \mu_l/\mu_g$	
ρ	density	kg/m^3

σ	surface tension coefficient	N/m
τ_{sh}	Shear breakup timescale $\tau_{sh} = D\sqrt{\varepsilon}/U$	-

789

Subscripts

Symbol	Description
0	initial
g	gas
l	liquid
rel	relative
x,y,z	coordinates

790

Abbreviations

Symbol	Description
BFW	Body Force Weighted
CFD	Computational Fluid Dynamics
CICSAM	Compressive Interface Capturing scheme for Arbitrary Meshes
CLSVOF	Coupled Level-Set VOF
cpR	Cells per Radius
DNS	Direct numerical simulation
PISO	Pressure-Implicit with Splitting of Operators
PIV	Particle Image Velocimetry
PRESTO	PREssure STaggering Option
UDF	User Defined Function
VOF	Volume of Fluid

791

792 # 7 References

793

794 Aalburg, C., 2002. Deformation and breakup of round drop and nonturbulent liquid jets in
795 uniform crossflows, Aerospace Engineering and Scientic Computing. University of Michigan.

796 ANSYS®FLUENT, 2012. Release 14.5, Theory Guide.

797 Barth, T., Jespersen, D., 1989. The design and application of upwind schemes on unstructured
798 meshes, 27th Aerospace Sciences Meeting. American Institute of Aeronautics and
799 Astronautics.

800 Cao, X.-K., Sun, Z.-G., Li, W.-F., Liu, H.-F., Yu, Z.-H., 2007. A new breakup regime of
801 liquid drops identified in a continuous and uniform air jet flow. Physics of Fluids 19, 057103.

802 Chou, W.H., Faeth, G.M., 1998. Temporal properties of secondary drop breakup in the bag
803 breakup regime. International Journal of Multiphase Flow 24, 889-912.

804 Chou, W.H., Hsiang, L.P., Faeth, G.M., 1997. Temporal properties of drop breakup in the
805 shear breakup regime. International Journal of Multiphase Flow 23, 651-669.

806 Clift, R., Grace, J.R., Weber, M.E., 1978. Bubbles, drops and particles. Academic Press, New
807 York.

808 Dai, Z., Faeth, G.M., 2001. Temporal properties of secondary drop breakup in the multimode
809 breakup regime. International Journal of Multiphase Flow 27, 217-236.

810 Faeth, G.M., Hsiang, L.P., Wu, P.K., 1995. Structure and breakup properties of sprays.
811 International Journal of Multiphase Flow 21, Supplement, 99-127.

812 Flock, A.K., Guildenbecher, D.R., Chen, J., Sojka, P.E., Bauer, H.J., 2012. Experimental
813 statistics of droplet trajectory and air flow during aerodynamic fragmentation of liquid drops.
814 International Journal of Multiphase Flow 47, 37-49.

815 Gelfand, B.E., 1996. Droplet breakup phenomena in flows with velocity lag. Progress in
816 Energy and Combustion Science 22, 201-265.

817 Gu, C.Y., 1991. Computation of flows with large body forces, in: Taylor, C., Chin, J.H.
818 (Eds.), Numerical Methods in Laminar and Turbulent Flow. Pineridge Press, Swansea, UK,
819 pp. 294–305.

820 Guildenbecher, D.R., López-Rivera, C., Sojka, P.E., 2009. Secondary atomization.
821 Experiments in Fluids 46, 371-402.

822 Guildenbecher, D.R., Sojka, P.E., 2011. EXPERIMENTAL INVESTIGATION OF
823 AERODYNAMIC FRAGMENTATION OF LIQUID DROPS MODIFIED BY
824 ELECTROSTATIC SURFACE CHARGE. Atomization and Sprays 21, 139-147.

825 Han, J., Tryggvason, G., 2001. Secondary breakup of axisymmetric liquid drops. II. Impulsive
826 acceleration. Physics of Fluids 13, 1554-1565.

827 Hsiang, L.P., Faeth, G.M., 1992. Near-limit drop deformation and secondary breakup.
828 International Journal of Multiphase Flow 18, 635-652.

829 Hsiang, L.P., Faeth, G.M., 1993. Drop properties after secondary breakup. International
830 Journal of Multiphase Flow 19, 721-735.

831 Hsiang, L.P., Faeth, G.M., 1995. Drop deformation and breakup due to shock wave and
832 steady disturbances. International Journal of Multiphase Flow 21, 545-560.

833 Issa, R.I., 1986. Solution of implicitly discretised fluid flow equations by operator-splitting.
834 Journal of Computational Physics 62, 40-65.

835 Jain, M., Prakash, R.S., Tomar, G., Ravikrishna, R.V., 2015. Secondary breakup of a drop at
836 moderate Weber numbers. Proceedings of the Royal Society of London A: Mathematical,
837 Physical and Engineering Sciences 471.

838 Jalaal, M., Mehravaran, K., 2012. Fragmentation of falling liquid droplets in bag breakup
839 mode. International Journal of Multiphase Flow 47, 115-132.

840 Jalaal, M., Mehravaran, K., 2014. Transient growth of droplet instabilities in a stream.
841 Physics of Fluids 26, 012101.

842 Kékesi, T., Amberg, G., Prahl Wittberg, L., 2014. Drop deformation and breakup.
843 International Journal of Multiphase Flow 66, 1-10.

844 Khare, P., Yang, V., 2013. Drag Coefficients of Deforming and Fragmenting Liquid Droplets,
845 ILASS Americas.

846 Khosla, S., Smith, C.E., 2006. Detailed Understanding of Drop Atomization by Gas
847 Crossflow Using the Volume of Fluid Method, ILASS Americas, Toronto, Canada.

848 Krzeczkowski, S.A., 1980. Measurement of liquid droplet disintegration mechanisms.
849 International Journal of Multiphase Flow 6, 227-239.

850 Lee, C.H., Reitz, R.D., 2000. An experimental study of the effect of gas density on the
851 distortion and breakup mechanism of drops in high speed gas stream. International Journal of
852 Multiphase Flow 26, 229-244.

853 Liu, Z., Reitz, R.D., 1997. An analysis of the distortion and breakup mechanisms of high
854 speed liquid drops. International Journal of Multiphase Flow 23, 631-650.

855 Malgarinos, I., Nikolopoulos, N., Gavaises, M., 2015. Coupling a local adaptive grid
856 refinement technique with an interface sharpening scheme for the simulation of two-phase
857 flow and free-surface flows using VOF methodology. Journal of Computational Physics 300,
858 732-753.

859 Malgarinos, I., Nikolopoulos, N., Marengo, M., Antonini, C., Gavaises, M., 2014. VOF
860 simulations of the contact angle dynamics during the drop spreading: Standard models and a
861 new wetting force model. Advances in Colloid and Interface Science 212, 1-20.

862 Michaelides, E.E., 2006. Particles, bubbles & drops: their motion, heat and mass transfer.
863 World Scientific.

864 Nicholls, J.A., Ranger, A.A., 1969. Aerodynamic shattering of liquid drops. AIAA Journal 7,
865 285-290.

866 Opfer, L., Roisman, I.V., Tropea, C., 2012. Aerodynamic Fragmentation of Drops: Dynamics
867 of the Liquid Bag, ICLASS 2012, Heidelberg, Germany.

868 Opfer, L., Roisman, I.V., Venzmer, J., Klostermann, M., Tropea, C., 2014. Droplet-air
869 collision dynamics: Evolution of the film thickness. Physical Review E 89, 013023.

870 Patankar, S.V., 1980. Numerical Heat Transfer and Fluid Flow. Hemisphere, Washington,
871 DC.

872 Pilch, M., Erdman, C., 1987. Use of breakup time data and velocity history data to predict the
873 maximum size of stable fragments for acceleration-induced breakup of a liquid drop.
874 International Journal of Multiphase Flow 13, 741-757.

875 Quan, S., 2009. Dynamics of Droplets Impulsively Accelerated by Gaseous Flow: A
876 Numerical Investigation, ICLASS 2009, Vail, Colorado, USA.

877 Quan, S., Schmidt, D.P., 2006. Direct numerical study of a liquid droplet impulsively
878 accelerated by gaseous flow. Physics of Fluids 18, 103103.

879 Strotos, G., Malgarinos, I., Nikolopoulos, N., Papadopoulos, K., Theodorakakos, A.,
880 Gavaises, M., 2015. Performance of VOF methodology in predicting the deformation and
881 breakup of impulsively accelerated droplets 13th ICLASS, Tainan, Taiwan.

882 Tavangar, S., Hashemabadi, S.H., Saberimoghadam, A., 2014. Reduction of Parasitic
883 Currents in Simulation of Droplet Secondary Breakup with Density Ratio Higher than 60 by
884 InterDyMFoam. Iranian Journal of Chemical Engineering 11, 29-42.

885 Theodorakakos, A., Bergeles, G., 2004. Simulation of sharp gas–liquid interface using VOF
886 method and adaptive grid local refinement around the interface. International Journal for
887 Numerical Methods in Fluids 45, 421-439.

888 Theofanous, T.G., 2011. Aerobreakup of Newtonian and Viscoelastic Liquids. Annual
889 Review of Fluid Mechanics 43, 661-690.

890 Ubbink, O., 1997. Numerical prediction of two fluid systems with sharp interfaces. PhD
891 Thesis, Department of Mechanical Engineering, Imperial College of Science, Technology &
892 Medicine,University of London.

893 Wadhwa, A.R., Magi, V., Abraham, J., 2007. Transient deformation and drag of decelerating
894 drops in axisymmetric flows. Physics of Fluids 19, 113301.

895 Xiao, F., 2012. Large Eddy Simulation of liquid jet primary breakup. PhD Thesis,
896 Loughborough University.

897 Xiao, F., Dianat, M., McGuirk, J.J., 2012. LES of Single Droplet and Liquid Jet Primary
898 Break-up Using a Coupled Level Set/Volume of Fluid Method, 12th ICLASS, Heidelberg,
899 Germany.

900 Yang, W., Jia, M., Sun, K., Wang, T., 2016. Influence of density ratio on the secondary
901 atomization of liquid droplets under highly unstable conditions. Fuel 174, 25-35.

902 Zhao, H., Liu, H.-F., Li, W.-F., Xu, J.-L., 2010. Morphological classification of low viscosity
903 drop bag breakup in a continuous air jet stream. Physics of Fluids 22, 114103.

904 Zhao, H., Liu, H.-F., Xu, J.-L., Li, W.-F., Lin, K.-F., 2013. Temporal properties of secondary
905 drop breakup in the bag-stamen breakup regime. Physics of Fluids 25, 054102.

906

8 Figure Captions

Fig.1: (a) *We* numbers ranges corresponding to the basic breakup regimes (*Oh*<0.1). The breakup modes between the bag breakup and the sheet thinning breakup have been merged into the "intermediate" breakup. In (b) the breakup modes observed into the "intermediate" breakup mode are shown. The data presented in (a) have been grouped into review studies, shock tube (S.T.) and continuous air jet (C.A.J.) experiments.

Fig.2: (a) sketch of the experimental setup of (Flock et al., 2012), (b) computational domain and boundary conditions used for the 3D simulations, (c) computational grid at the symmetry plane.

Fig.3: Computational grid and boundary conditions for the 2D simulations. (5 levels of local grid refinement, 96cpR)

Fig.4: Temporal evolution of the droplet dimensions and droplet shapes (in intervals of 2ms) for three different grid densities (*We*=13, 2D axisymmetric domain). The last droplet shape corresponds to 11ms which is approximately the time of breakup. The bottom row shows a three-dimensional representation of the droplet shapes by revolving the 0.5 VOF iso-value.

928

929 Fig.5: Effect of implicit VOF solution in the 2D predictions of the bag breakup case
930 (*We*=13) with the Compressive VOF discretization scheme and the sharpening
931 algorithm.

932

933 Fig.6: Temporal evolution of droplet dimensions and droplet shape evolution in 1ms
934 intervals for three different grid densities (*We*=32, 2D axisymmetric domain). The
935 bottom row shows a three-dimensional representation of the droplet shapes by
936 revolving the 0.5 VOF iso-value.

937

938 Fig.7: Predictions of the 3D model for the bag breakup case (*We*=13) for the droplet
939 dimensions (a) and the droplet trajectory (b).

940

941 Fig.8: Predictions of the 3D model for the bag breakup case (*We*=13) for the droplet
942 shape and trajectory (in intervals of 2ms). At the right part, the experimental photos of
943 (Flock et al., 2012) corresponding to Figure 10 of their paper, are also shown; their
944 experimental time has been shifted by 1ms.

945

946 Fig.9: Different views of the droplet shape for the bag breakup case (*We*=13) in
947 intervals of 2ms for the case of explicit VOF solution with the BFW scheme.

948

949 Fig.10: Predicted pressure and velocity field for the bag breakup case (*We*=13) using
950 the PRESTO scheme.

951

952 Fig.11: Predicted pressure and velocity field for the bag breakup case (*We*=13) using
953 the BFW scheme.

954

955 Fig.12: (a) Averaged and (b) instantaneous velocity field at 7ms obtained with the
956 PIV technique in (Flock et al., 2012) for the bag breakup case (*We*=13).

957

958 Fig.13: Predictions of the 3D model for the sheet thinning breakup case (*We*=32) for
959 the droplet dimensions (a) and the droplet trajectory (b).

960

961 Fig.14: Predictions of the 3D model for the sheet thinning breakup case (*We*=32) for
962 the droplet shape and trajectory (in intervals of 1ms).

963

964 Fig.15: Different views of the droplet shape in intervals of 1ms for the case of explicit
965 VOF solution with the PRESTO scheme for the sheet thinning breakup case (*We*=32).

966

967 Fig.16: Different views of the droplet shape in intervals of 1ms for the case of explicit
968 VOF solution with the BFW scheme for the sheet thinning breakup case (*We*=32).

Fig.17: Predicted absolute velocity field for the sheet thinning breakup case (*We*=32) using explicit VOF for (a) the PRESTO and (b) the BFW scheme.

Fig.18: Averaged (a) and instantaneous (b) velocity field at 4ms obtained with the PIV technique in (Flock et al., 2012) for the sheet thinning breakup case (*We*=32).

Fig.19: Parametric study for the effect of *We* number (2D axisymmetric simulations). (a) Droplet shapes corresponding to time intervals of 0.05τsh, (b) cross-stream droplet deformation, (c) droplet velocity.

Fig.20: (a) experimental photos of (Zhao et al., 2013) for the dual-bag breakup of water droplets for *We*=29, (b) present 3D predictions for *We*=32 with the BFW pressure scheme.

9 Tables

Table 1: List of the numerical settings adopted for the explicit and the implicit VOF solver.

Table 2: List of the assumptions adopted for the 2D and the 3D model.

989

990 Table 3: List of the cases examined.